ChemPubSoc Europe

DOI: 10.1002/celc.201800152

CHEMELECTROCHEM Articles

Highly Reversible Water Oxidation at Ordered Nanoporous Iridium Electrodes Based on an Original Atomic Layer Deposition

Stefanie Schlicht,[a] Sandra Haschke,[a] Vladimir Mikhailovskii,[b] Alina Manshina,[c] and Julien Bachmann*[a]

Nanoporous iridium electrodes are prepared and electrochemically investigated towards the water oxidation (oxygen evolution) reaction. The preparation is based on 'anodic' aluminum oxide templates, which provide straight, cylindrical nanopores. Their walls are coated using atomic layer deposition (ALD) with a newly developed reaction which results in a metallic iridium layer. The ALD film growth is quantified by spectroscopic ellipsometry and X-ray reflectometry. The morphology and composition of the electrodes are characterized by scanning electron microscopy, energy-dispersive X-ray spectroscopy, and X-ray diffraction. Their catalytic activity is quantified for various pore geometries by cyclic voltammetry, steady-state electrolysis, and electrochemical impedance spectroscopy. With an optimal pore length of $L \approx 17$–20 μm, we achieve current densities of $J = 0.28$ mA cm^{-2} at pH 5 and $J = 2.4$ mA cm^{-2} at pH 1. This platform is particularly competitive for achieving moderate current densities at very low overpotentials, that is, for a high degree of reversibility in energy storage.

1. Introduction

A major avenue of current research is the conversion of solar energy to chemical energy via electrochemical splitting of water. The oxidative half-reaction is the four-electron evolution of dioxygen, which represents the kinetic bottleneck of the overall reaction.[1] In industrial electrolysis optimized towards throughput of hydrogen as a commodity reagent at minimized capital expenditure, the kinetic limitation is overcome by large applied overpotentials (typically $\eta = 0.6$ V and more) that yield current densities in the range of 1–10 A cm^{-2}.[2–5] In this case, however, the energy source must be inexpensive. In academic research, the overpotential needed to reach current densities up to 10 mA cm^{-2} is often taken as a performance quantifier, and the state of the art lies around more moderate $\eta = 0.3$ V.[6–9] However, if water splitting is to be used as an energy storage method, then reversibility must be considered as the most important performance parameter. In this context, an overpotential of $\eta = 0.3$ V already represents losses of 24% (based on the thermodynamic voltage of 1.23 V defining $\eta = 0.0$ V). Thus, the most crucial requirement for water splitting to become a viable energy storage strategy is the possibility of operating water oxidation under even lower overpotentials (on the order of $\eta = 0.1$–0.2 V, that is, 8–16% energy loss due to voltage) at practical current densities in the mA cm^{-2} range.

The slow kinetics at low η can be improved in two distinct and complementary ways, namely, by varying the material and by optimizing the electrode geometry. Regarding the choice of electrode material, the 'volcano' plot highlights the noble metal compounds RuO_2, PtO_2 and IrO_2 as the most active for oxygen evolution catalysis due to optimal adsorption energies.[10–12] Although these catalysts are quite expensive, they still represent the state of the art in acidic electrolysis to date.[13,14] Herein, we focus on the second aspect, namely the electrode surface geometry, in order to optimize electrocatalytic turnover at the noble metal (Ir) catalyst surface by facilitating transport in the electrolyte.

Ir and IrO_2 electrodes have been produced by a variety of methods, for instance electrochemical synthesis,[15] hydrothermal,[16] sol-gel,[17,18] or wet chemical methods.[19] Additionally, chemical vapor deposition[20–23] and pulsed laser deposition[24,25] have been reported as thin film techniques. They are, however, not designed to coat highly porous substrates conformally. Thus, the present work focuses on atomic layer deposition (ALD) for the preparation of iridium electrodes with accurately defined and tunable pore geometry. ALD, which is defined by its self-limiting surface reaction mechanism, is uniquely capable of generating thin coatings not only on planar substrates but also nanostructured ones.[26–29] The combination of nanoporous aluminum oxide templates, which provide cylindrical pores of diameter and length tunable at will, with an iridium coating by

[a] S. Schlicht, S. Haschke, J. Bachmann
Departement of Chemistry and Pharmacy,
Friedrich-Alexander University Erlangen-Nürnberg,
Egerlandstrasse 1, 91058 Erlangen, Germany
E-mail: julien.bachmann@fau.de
[b] V. Mikhailovskii
Saint-Petersburg State University,
Interdisciplinary Resource Center for Nanotechnology,
Uljanovskaya 1, 198504 St. Petersburg, Russia
[c] A. Manshina
Saint-Petersburg State University,
Institute of Chemistry,
Universitetskii pr. 26, 198504 St. Petersburg, Russia

Supporting information for this article is available on the WWW under https://doi.org/10.1002/celc.201800152

ALD, operating as the catalyst for the oxygen evolution reaction (OER), represents a versatile method for preparing electrodes the surface geometry of which can be varied systematically.

We introduce a novel Ir ALD reaction and exploit it to investigate the electrochemical performance of nanoporous water oxidation electrodes as it depends on geometry systematically. As a result, we demonstrate that the reaction can be performed at very low overpotentials with moderate current densities ($J=2.4$ mA cm^{-2} at $\eta=0.24$ V, $J=0.43$ mA cm^{-2} at $\eta=0.14$ V and $J=0.34$ mA cm^{-2} at $\eta=0.04$ V) – such near-reversibility is of particular interest for energy storage.

2. Results and Discussion

The use of nanoporous 'anodic' aluminum oxide (AAO) templates offers the experimentalist two main adjustable parameters. First, the diameter of the well-ordered, straight cylindrical nanopores yielded by the electrochemical procedure can be tuned in a range of about 20 nm to 400 nm. Secondly, the length of the pores can be varied between 0.5 μm and 100 μm typically. Thus, this preparative method allows for the systematic tuning of the geometric surface area of an inert template. For generating a functional electrode, this template is superficially covered with an electrical contact layer of Au and Ni by sputter coating and subsequent galvanic plating, respectively. Finally, the inner walls of the nanoporous system are coated with a thin continuous layer of metallic Ir by ALD. This self-limiting surface chemical technique allows for the deposition of thin coatings in pores by repeating two complementary surface reactions in a cyclic manner until the desired thickness is reached. The overall preparative method is shown in Figure 1.

For the deposition of the iridium catalyst we developed a novel ALD reaction based on the commercially available precursor ethylcyclopentadienyl-1,3-cyclohexadiene iridium (I), (EtCp)Ir(CHD). To the best of our knowledge, this precursor has only been used for MOCVD to date.[30–32] Compared to the standard ALD precursor Ir(acac)$_3$ (iridium (III) acetylacetonate), (EtCp)Ir(CHD) provides a higher vapor pressure, which benefits the coating of deep

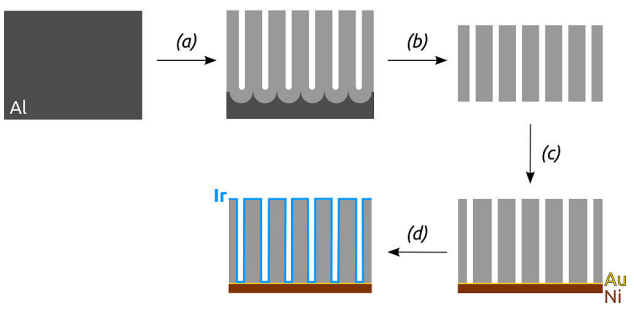

Figure 1. Preparation of the nanoporous iridium electrodes. a) Anodization of Al sheets yields ordered cylindrical pores. b) Free-standing nanopores with defined diameter and pore length are obtained after removal of Al backside and aluminum oxide barrier layer. c) Coating the template with an Au and Ni electrical contact is performed by sputter coating and galvanic plating. d) Atomic layer deposition coats the iridium catalyst along the inner pore walls.

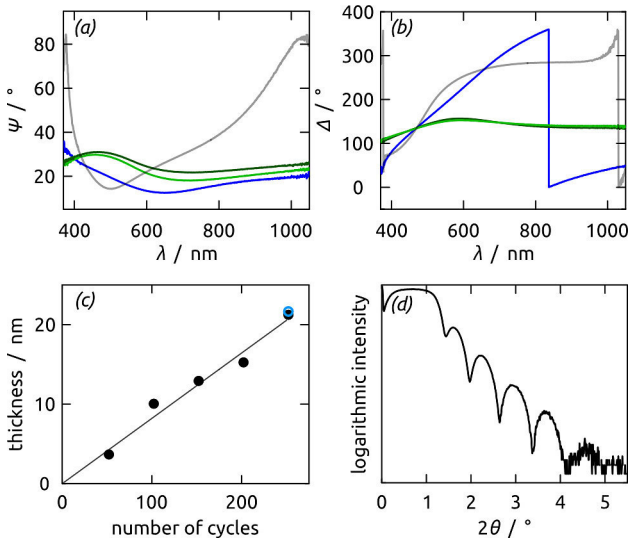

Figure 2. Iridium film growth characterization. Spectroscopic ellipsometry data [amplitude (a) and phase difference (b)] obtained from a Si wafer covered with ITO and with varying iridium coatings: 0 ALD cycle (gray), 50 ALD cycles (blue), 150 cycles (light green) and 200 cycles (dark green). c) ALD growth curve, showing the increase in iridium film thickness to be in direct proportionality to the number of ALD cycles performed. The blue circle results from X-ray reflectometry (XRR), black disks have been obtained by spectroscopic ellipsometry. d) XRR data recorded on a Si wafer coated with Al_2O_3 as an adhesion layer then 250 cycles of iridium.

nanopores. When (EtCp)Ir(CHD) and ozone (O_3) are pulsed in alternating fashion on planar substrates (Si wafers coated with alumina or indium tin oxide (ITO)), a film growth is observed by spectroscopic ellipsometry: Figure 2a,b exhibit clear changes in the ellipsometric curves after various ALD cycle numbers, and their fit to a model (Ir/ITO/SiO_2/Si stack) yields a growth rate of 0.9 Å/cycle, confirmed by X-ray reflectometry (Figure 2c,d). The ALD nature of this reaction is proven by varying the amount of precursor delivered at each cycle. When the number of 500 ms long micropulses of (EtCp)Ir(CHD) vapor delivered at each cycle is varied from 1 to 8, the saturation behavior that serves as a hallmark for the self-limiting nature of ALD[26–29] is achieved with 4 pulses per cycle (Figure 3a).

The chemical identity of the black deposit is investigated on nanoporous samples coated with the same ALD method. X-ray

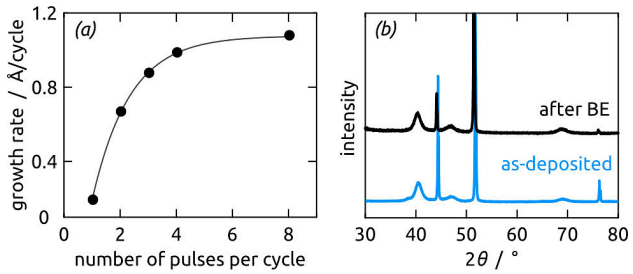

Figure 3. a) Proof of self-limiting surface chemistry, establishing the ALD nature of the Ir thin film deposition performed: the growth rate saturates as the precursor dosage is increased. b) X-ray diffraction pattern obtained from coated AAO before (blue) and after (black) electrochemical investigation.

diffraction (Figure 3b) yields prominent peaks at 40.5°, 46.9° and 69.1°, which can be attributed to the (111), (200) and (220) reflexes of crystalline and metallic iridium, COD 9008470.[33,34] Their significant width is a result of a small crystal size. Using the Scherrer formula on these three peaks, a calculated crystallite size of 75(±3) Å is obtained. The other peaks located at 44.4°, 51.8° and 76.3° are due to the Au and Ni present in the contact layer, respectively (COD 1100138 and 2100649). This metallic state, which also causes the black color of the samples (Figure 4a,b), is obtained instead of IrO_2 despite the strong oxidant used as ALD precursor (O_3). This behavior, however, is consistent with a large number of ALD reactivity studies in the noble metal field. Depending on thermodynamics and temperature, the metastable oxide, present at the surface and necessary for surface reactivity, decomposes to gaseous dioxygen and bulk elemental metal.[35–37]

Figure 4c–e display scanning electron micrographs of the nanostructured electrodes after coating with iridium in top view. All pores with a diameter of about 350 nm are well ordered in a hexagonal arrangement. Energy-dispersive X-ray (EDX) spectroscopic analysis exhibits signals for the elements expected: Ir as the catalyst, Al and O in the AAO template, as well as Au and Ni from the electrical contact (Figure 4f).

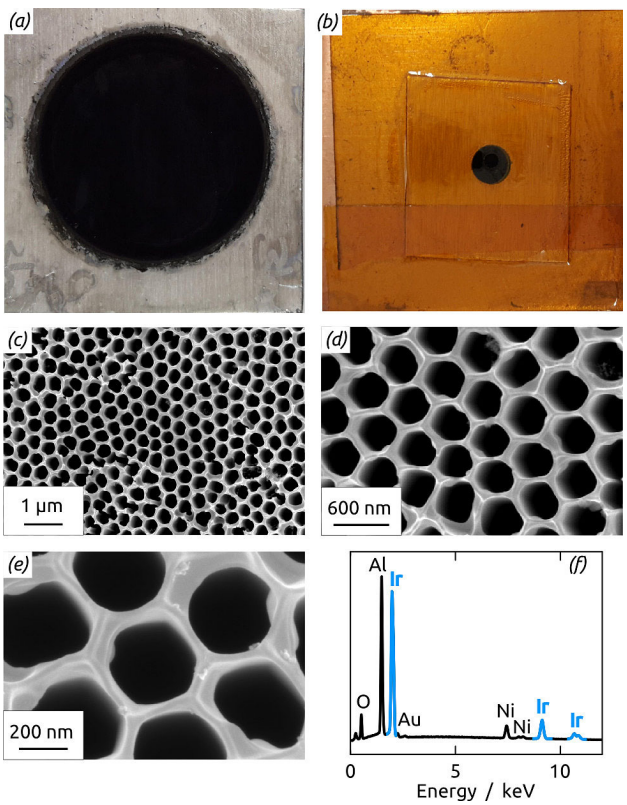

Figure 4. Characterization of nanoporous Ir samples. a) Photograph of a sample after all preparation steps described in Figure 1. The iridium coating is homogenous throughout the entire Al_2O_3 template (14 mm diameter). b) Sample for electrochemical studies. A small piece is placed on a Cu plate using Cu tape and masked with Kapton® tape with a circular opening of $d = 1$ mm. c–e) Scanning electron micrographs (in top view) of anodic aluminum oxide membranes coated with Ir by 250 cycles of atomic layer deposition, under different magnifications. f) Energy-dispersive X-ray analysis proving the presence of iridium.

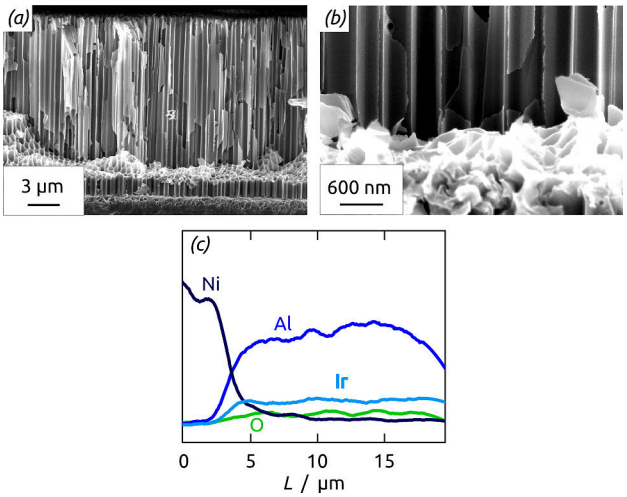

Figure 5. a, b) Scanning electron microscopy images of a functional electrode in cross-section at two different magnifications. In low magnification, the contrast is homogeneous throughout the thickness of the Ir/Al_2O_3 composite. In high magnification, the Ir coating is discernible. c) EDX analysis recorded in cross-section along one pore length yields a constant Ir signal from the top to the bottom of the AAO.

The homogeneity of the iridium catalyst deposition along the nanopores' depth is proven by SEM and EDX analysis recorded on the cross-section (Figure 5). A smooth iridium layer along the inner walls of the template is visible at high magnification, Figure 5b. Its continuity from one pore extremity to the other is demonstrated by the EDX profile recorded along the pore length, which yields a homogenous iridium signal from the bottom (Ni segments) to the top of the AAO template (Figure 5c). The Ni contact, in a contrasting manner, is localized on one side of the sample, as it should be.

Let us now quantify the electrocatalytic oxygen evolution activity of our nanoporous iridium electrodes by cyclic voltammetry (CV), steady-state electrolysis and electrochemical impedance spectroscopy (EIS). The samples for electrochemical investigation were laser-cut to define the macroscopic surface area accurately and placed on Cu plates using double-sided adhesive Cu tape (Figure 4b). All electrochemical measurements were recorded either in Na_2HPO_4/NaH_2PO_4 at pH 5 or in H_2SO_4 at pH 1. Starting at the open-circuit potential (OCP), the cyclic voltammogram presents the expected exponential increase of current density resulting from the evolution of dioxygen from water (Figure S1 in the Supporting Information). Absolute values of the current density lie an order of magnitude higher than with planar samples measured as references. The CV displays a slightly hysteretic behavior caused by charging effects of the electrode surface (capacitive current). The forward scan of the first CV cycle (inset of Figure S1) shows an anodic hydrogen desorption current at about +0.1 V,[38,39] followed by the formation of Ir(III) oxide and hydrous Ir(IV) oxide species in range of +0.6 V to +1.1 V.[40,41] The hydrogen adatom adsorption/desorption peak is no longer visible in subsequent measurements. These observations are consistent with the

formation of a pure metallic Ir by ALD, followed by electrochemical surface oxidation, which is not reversed within the range of potentials applied. After the initial cycle, subsequent voltammetric cycling as well as steady-state electrolyses for several hours cause no apparent macroscopic change of the samples. The XRD (Figure 3b) displays no significant change of the pattern, either, which proves the stability of our catalyst in electrochemical conditions. The capacitive CV current is slightly increased, probably due to surface roughening. The evolution of dioxygen at elevated applied potentials is proven by measurements performed with an O_2 sensor (Figure S2 in the Supporting Information).

Our preparative strategy allows us to investigate the impact of the electrode's geometric surface area on the water oxidation catalysis performance. We are able to tune the surface area systematically by varying the pore length L while maintaining a constant pore diameter. The dependence of the current density on the pore length is demonstrated in Figure 6a. Upon pore elongation from 0 to 17 μm (pH 5) or 20 μm (pH 1), the current increases linearly, whereas further pore elongation up to 27 μm results in an activity loss. This effect is observed for both pH values 5 and 1, albeit at very different scales of the absolute current density. It can be interpreted by transport effects, which become limiting beyond $L \approx 17$–20 μm. The influence of transport in these nanostructured iridium electrodes is also observable in the Tafel plots (Figure S3 in the Supporting Information). The Tafel slopes of our nanoporous samples are always significantly larger than most planar electrodes: our $L = 17$ μm sample exhibits 160 mV per decade (Figure 6b). This is due to diffusion, which becomes more limiting as overpotentials (which tend to increase current densities) are augmented.

The effects of beneficial surface area enhancement and detrimental transport limitations in steady-state electrolysis upon pore elongation are visible in electrochemical impedance spectroscopy (EIS) analysis. The data collected at +1.0 V between 100 kHz and 0.05 Hz for different pore lengths and the corresponding fits created from an equivalent circuit model are shown in Figure 7a as Nyquist plots. The model consists of a single Randles cell, with a charge transfer resistance R_{ct} in parallel with a constant phase element of impedance Y, the use of which is often associated with electrode porosity, roughness or inhomogeneous potential distribution.[48] An element R_u represents the series resistance. Letting all parameters vary in the fit, the exponent of the constant-phase element, alpha, varies in the range $0.9 < \alpha < 1.0$, indicating a smooth surface. This very narrow range of α values enables us to fix it to $\alpha = 0.95$ for subsequent fits, for the purpose of comparing the samples (Table 1).

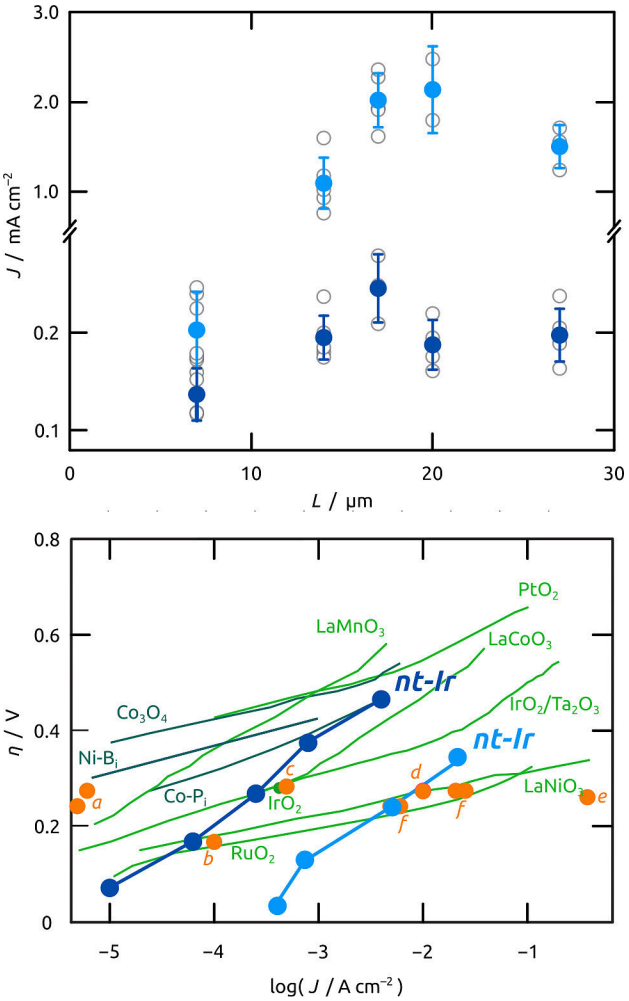

Figure 6. Upper panel, dependence of the current density J on the pore length for two distinct pH value at constant overpotential $\eta = 0.26$ V (pH 5, dark blue data points) and $\eta = 0.24$ V (pH 1, light blue data points). The current density increases until a pore length of $L \approx 17$–20 μm. Further pore elongation results in an activity loss. Individual samples of nominally identical geometry are represented with empty gray circles, whereas their averages are given (with error bars) in full disks. Lower panel, Tafel plot comparing the performance (in terms of current density J and overpotential η) of one nanoporous iridium electrode ($L = 17$ μm) at pH 5 (dark blue) and pH 1 (light blue) with the state of the art. Planar electrode materials used at $pH \leq 1$ or $pH \geq 13$ are represented in light green, planar electrodes at $5 \leq pH \leq 9$ in dark green.[10] Nanostructured IrO_2-based systems (at $pH \leq 1$ or $pH \geq 13$) are given by orange data points: a) Ref. [42], b) Ref. [43], c) Ref. [44], d) Ref. [45], e) Ref. [46], f).Ref. [47].

Table 1. EIS analysis of the nanoporous iridium electrodes with different pore lengths L according to the presented model (at pH 1 and $E = 1.0$ V vs. Ag/AgCl). The lowest value of R_{ct} is obtained with a pore length of $L = 17$ μm.

L [μm]	R_u [Ω]	R_{ct} [kΩ]	α (set)	Y [10^{-6} S s$^{\alpha}$]
7	210	62.7	0.95	76
14	157	37.6	0.95	206
17	162	27.9	0.95	290
20	175	39.7	0.95	189
27	162	48.5	0.95	302

The charge transfer resistance starts by decreasing as L increases, as expected based on the geometric surface area (Figure 7b and Table 1, pH 1). The capacity increases in direct proportion to the geometric surface area, which proves that the full pore length is electrically contacted, therefore, that the metallic layer is continuous. However, the R_{ct} value is lowest for the $L = 17$ μm sample, which presents the smallest semicircle (Figure 7a, Table 1). Beyond $L = 17$ μm, R_{ct} no longer decreases

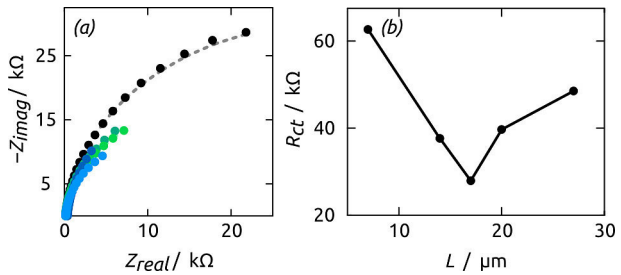

Figure 7. a) Electrochemical impedance spectroscopy (at $E = 1.0$ V vs. Ag/AgCl) of iridium electrodes with different pore lengths: 7 µm (black), 14 µm (dark green), 17 µm (light blue), 20 µm (light green) and 27 µm (dark blue). b) Dependence of charge transfer resistance R_{ct} on pore length L. The sample with pores $L = 17$ µm yields the lowest charge transfer resistance $R_{ct} = 27.9$ kΩ.

and Y no longer increases. This is an indication that for very long pores, only a fraction of the total surface turns over at its maximal possible rate, which we attribute to transport limitation.

A final note concerns the stability of our system. We observe no significant structural reorganization (by SEM) after 8 to 12 hours of either continuous electrolysis or various investigations including voltammetry and EIS (Figure S4 to be compared with Figure 4). One time-current trace for a 12-hour electrolysis is presented in the Supporting Information (Figure S5). The metallic nature of the bulk iridium is also maintained after electrochemical treatment, as observed by XRD (Figure 3b).

3. Conclusions

A preparative method is now available to the electrochemical community for generating iridium electrodes with highly controlled surface geometry. It consists of a parallel array of straight, cylindrical pores the diameter and length of which can be set to values $20\ \text{nm} \leq d \leq 350\ \text{nm}$ and $0.5\ \mu\text{m} \leq L \leq 100\ \mu\text{m}$, respectively, at the experimentalist's discretion. The method bases on a novel ALD reaction for Ir, which advantageously replaces earlier methods as it allows for the reproducible and fast growth of homogeneous coatings in deep pores.

This porous system represents a platform on which to study geometric effects on electrocatalytic transformations in a systematic manner. In particular, we have already established the crossover from surface limitation to transport limitation in the oxygen evolution reaction, which amounts to a precise optimization of the water splitting process.

The $10\ \text{mA cm}^{-2}$ performance is competitive with the best reported to date ($\eta < 0.3$ V), albeit very large current densities are difficult to reach. Conversely, however, the samples provide moderate current densities at very low overpotentials. In other words, they allow one to perform the storage of electrical energy in chemical form (as fuels) under conditions of high reversibility (with low energy losses). Further work will explore the minimization of noble metal loading in this splendidly controlled and highly promising system.

Experimental Section

Materials

Chemicals were purchased from Strem, VWR or Sigma Aldrich and used as received. Water was purified in a Millipore Direct-Q system. Aluminum plates (99.99%) were obtained from SmartMembranes. The Au sputter target was supplied by Stanford Advanced Materials. Si wafer covered with an oxide layer were ordered from Silicon Materials Inc.

Preparation of Nanoporous Templates

The nanoporous aluminum oxide (AAO) templates were prepared according to the usual two-step anodization procedure.[49,50] For the electrochemical oxide formation, aluminum sheets with a size of approximately ~5 cm^2 were placed in home-made PVC beakers with four circular openings and held between an O-ring and a copper plate serving as the electrical contact. Each beaker was closed with a metal housing equipped with a silver wire as the counter-electrode and a mechanical stirrer. First, the Al sheets were electropolished in a cooled mixture of perchloric acid and ethanol (v/v 1:3) under an applied potential of +20 V for 7 min. A first anodization was performed in 0.5 wt.% phosphoric acid under +195 V for 1 h at 0 °C, then for an additional 23 h in 1.0 wt.%. The sacrificial disordered oxide layer obtained was then removed by using chromic acid (2% H_2CrO_4 in H_3PO_4) at 45 °C for 23 h. The second anodization was subsequently carried out in 0.5 wt.% phosphoric acid under a potential of +195 V for 1 h and subsequently for 2 h, 5 h, 7 h, 9 h or 11 h in 1.0 wt.% phosphoric acid. The following steps include the removal of the Al backside with copper chloride solution (0.7 M in 10% HCl) and the removal of the aluminum oxide barrier layer by submerging the samples into 10 wt.% phosphoric acid for 36–46 min.

Preparation of Electrodes

The AAO template was coated with an Au layer of 100 nm with a Torr CRC 622 sputter coater. The contact layer was then thickened by Ni galvanic plating in a diluted Watts electrolyte (0.285 M $NiSO_4.6H_2O$, 0.0475 M $NiCl_2.6H_2O$, 0.5 M H_3BO_3) under −2.3 V in a two-electrode setup for 3 h. The last step was the deposition of iridium along the inner walls of the AAO template by atomic layer deposition using a commercial Gemstar-6 ALD reactor from Arradiance. Ethylcyclopentadienyl-1,3-cyclohexadiene-iridium (I) ((EtCp)Ir(CHD) from Strem) and ozone were used as precursors. Ozone was produced from oxygen in an ozone generator model BMT 803N. The (EtCp)Ir(CHD) precursor bottle was heated to 90 °C and the deposition was carried out at 220 °C. For the electrochemical measurements the samples were laser-cut with a GCC LaserPro in small circular pieces and glued onto copper plates using double-sided copper tape. A mask with a circular opening of $d = 1$ mm made of polyamide tape (Kapton®) was used in order to define an accurate electrode surface area.

Characterization

The morphology of the nanoporous iridium electrodes was investigated by scanning electron microscopy using a Zeiss Merlin field-emission microscope equipped with Oxford Instruments INCA A-Act EDX system. X-ray diffraction and X-ray reflectivity were performed on a Bruker D8 Advance equipped with a Cu K_α source and LynxEye XE T detector. The thickness of the iridium layer was measured by spectroscopic ellipsometry using a SENpro by Sentech.

Electrochemical Studies

All electrochemical measurements were performed in a three-electrode setup with an Ag/AgCl reference electrode with a stablepotential of +0.20 V vs NHE and Pt mesh as the counter-electrode. The data of cyclic voltammetry (CV), steady-state electrolysis (BE) and electrochemical impedance spectroscopy (EIS) were recorded either in 0.1 M NaH_2PO_4/Na_2HPO_4 (pH 5) or in 0.1 M H_2SO_4 (pH 1) using a Gamry Interface 1000 potentiostat. CV were recorded starting at the open circuit potential between 0.0 V and +1.4 V (vs. Ag/AgCl). The potential applied for steady-state electrolyses was varied between +0.8 V and +1.4 V (overpotentials $\eta = 0.065$ V to 0.665 V, pH 5 and $\eta = 0.041$ V to 0.341 V, pH 1). EIS was performed with an amplitude of 10 mA from 100 kHz to 0.05 Hz at +1.0 V. Direct quantification of the dioxygen evolved was performed with an optrode model Visiferm DO 160 by Hamilton.

Acknowledgements

This research was funded by the German Ministry of Education and Research (BMBF) in the project 'TubulAir±' (project number 03SF0436G), the German Academic Exchange Service (DAAD) via the German-Russian Interdisciplinary Research Center (G-RISC, project C-2016b-2), and the European Research Council with an ERC Consolidator Grant (grant number 647281, 'Solacylin'). We thank Prof. T. R. Cook for providing the graphic used in Figure 6. We acknowledge D. Döhler for his help with X-ray reflectometry.

Conflict of Interest

The authors declare no conflict of interest.

Keywords: Electrochemistry · catalysis · nanostructures · thin films · water splitting

[1] Y. Surendranath, M. Dincă, D. G. Nocera, *J. Am. Chem. Soc.* **2009**, *131*, 2615–2620.
[2] Y. Zeng, X. Guo, Z. Shao, H. Hu, W. Song, Z. Wang, H. Zhang, B. Yi, *J. Power Sources* **2017**, *342*, 947–955.
[3] M. G. Chourashiya, A. Urakawa, *J. Mater. Chem. A* **2017**, *5*, 4774–4778.
[4] S. Song, H. Zhang, X. Ma, Z. Shao, R. T. Baker, B. Yi, *Int. J. Hydrogen Energy* **2008**, *33*, 4955–4961.
[5] E. Antolini, *ACS Catal.* **2014**, *4*, 1426–1440.
[6] D.-Y. Kuo, J. K. Kawasaki, J. N. Nelson, J. Kloppenburg, G. Hautier, K. M. Shen, D. G. Schlom, J. Suntivich, *J. Am. Chem. Soc.* **2017**, *139*, 3473–3479.
[7] S. H. Lee, H. Lee, M. Cho, Y. Lee, *Carbon* **2017**, *115*, 50–58.
[8] D. Takimoto, K. Fukuda, S. Miyasaka, T. Ishida, Y. Ayato, D. Mochizuki, W. Shimizu, W. Sugimoto, *Electrocatalysis* **2017**, *8*, 144–150.
[9] M. Bernicke, E. Ortel, T. Reier, A. Bergmann, J. Ferreira de Araujo, P. Strasser, R. Kraehnert, *ChemSusChem* **2015**, *8*, 1908–1915.
[10] T. R. Cook, D. K. Dogutan, S. Y. Reece, Y Surendranath, T. S. Teets, D. G. Nocera, *Chem. Rev.* **2010**, *110*, 6474–6502.
[11] M. G. Walter, E. L. Warren, J. R. McKone, S. W. Boettcher, Q. Mi, E. A. Santori, N. S. Lewis, *Chem. Rev.*, **2010**, *110*, 64466473.
[12] S. Trasatti, *J. Electroanal. Chem. Interfacial Electrochem.* **1980**, *111*, 125–131.
[13] Y. Lee, J. Suntivich, K. J. May, E. E. Perry, Y. Shao-Horn, *J. Phys. Chem. Lett.* **2012**, *3*, 399–404.
[14] S. Cherevko, T. Reier, A. R. Zeradjanin, Z. Pawolek, P. Strasser, K. J. J. Mayrhofer, *Electrochem. Commun.* **2014**, *48*, 81–85.
[15] C. Zhao, H. Yu, Y. Li, X. Li, L. Ding, L. Fan, *J. Electroanal. Chem.* **2013**, *688*, 269–274.
[16] J. Tang, B. Kong, Y. Wang, M. Xu, Y. Wang, H. Wu, G. Zheng , *Nano Lett.* **2013**, *13*, 5350–5354.
[17] S. Ardizzone, C. L. Bianchi, L. Borgese, G. Cappelletti, C. Locatelli, A. Minguzzi, S. Rondinini, A. Vertova, P. C. Ricci, C. Cannas, A. Musinu, *J. Appl. Electrochem.* **2009**, *39*, 2093–2105.
[18] G. Wang, F. Cheng, Y. Yu, C. Liang, T. Xu, M. Pan, *Sci. China Chem.* **2013**, *56*, 131–136.
[19] J. Cheng, H. Zhang, H. Ma, H. Zhong, Y. Zou, *Electrochim. Acta* **2010**, *55*, 1855–1861.
[20] Y. L. Chen, C. C. Hsu, Y. H. Song, Y. Chi, A. J. Carty, S. M. Peng, G. H. Lee, *Chem. Vap. Deposition* **2006**, *12*, 442–447.
[21] R. S. Chen, Y. S. Huang, Y. M. Liang, D. S. Tsai, K. K. Tiong, *J. Alloys Compd.* **2004**, *383*, 273–276.
[22] R. S. Chen, Y.-S. Huang, Y.-M. Liang, D. S. Tsai, Y. Chi, J. J Kai, *J. Mater. Chem.* **2003**, *13*, 2525–2529.
[23] C. A. Chen, Y. M. Chen, Y. S. Huang, D. S. Tsai, K. K. Tiong, C. H. Du, *Nanotechnology* **2008**, *19*, 465607.
[24] L. M. Zhang, Y. S. Gong, C. B. Wang, Q. Shen, M. X. Xia, *Thin Solid Films* **2006**, *496*, 371–375.
[25] C. Wang, Y. Gong, Q. Shen, L. Zhang, *Appl. Surf. Sci.* **2006**, *253*, 2911–2914.
[26] J. Hämäläinen, M. Kemell, F. Munnik, U. Kreissig, M. Ritala, M. Leskelä, *Chem. Mater.* **2008**, *20*, 2903–2907.
[27] M. Leskelä, M. Ritala, *Angew. Chem. Int. Ed.* **2003**, *42*, 5548–5554.
[28] J. W. Elam, D. Routkevitch, P. P. Mardilovich, S. M. George, *Chem. Mater.* **2003**, *15*, 3507–3517.
[29] C. Detavernier, J. Dendooven, S. Pulinthanathu Sree, K. F. J. A. Martens, *Chem. Soc. Rev.* **2011**, *40*, 5242–5353.
[30] C.-P. Yeh, M. Lisker, J. Bläsing, O. Khorkhordin, B. Kalkofen, E. P. Burte, *Chem. Vap. Deposition* **2015**, *21*, 46–53.
[31] F. Hironori, W. Soichi, I. Naoya, S. Masaru, F. Taishi, K. Kazuhisa, O. Noriaki, *Jpn. J. Appl. Phys.* **2006**, *45*, 7354–7359.
[32] H. Fujisawa, M. Shimizu, H. Niu, S. Watari, N. Oshima, *J. Korean Phys. Soc.* **2005**, *46*, 176–179.
[33] J. Hamalainen, T. Hatanpaa, E. Puukilainen, T. Sajavaara, M. Ritala, M. Leskelä, *J. Mater. Chem.* **2011**, *21*, 16488–16493.
[34] X. Yan, Q. Zhang, X. Fan, *Mater. Lett.* **2007**, *61*, 216–218.
[35] L. Assaud, J. Schumacher, A. Tafel, S. Bochmann, S. Christiansen, J. Bachmann, *J. Mater. Chem. A* **2015**, *3*, 8450–8458.
[36] M. Leskela, T. Aaltonen, J. Hamalainen, A. Niskanen, M. Ritala, *Proc. Electrochem. Soc.* **2005**, 2005-09 (EUROCVD-15), 545–554.
[37] J. Hamalainen, M. Ritala, M. Leskela , *Chem. Mater.* **2014**, *26*, 786–801.
[38] S. Cherevko, S. Geiger, O. Kasian, A. Mingers, K. J. J. Mayrhofer, *J. Electroanal. Chem.* **2016**, *773*, 69–78.
[39] R. Woods, *J. Electroanal. Chem. Int.* **1974**, *49*, 217–226.
[40] T. Reier, M. Oezaslan, P. Strasser, *ACS Catal.* **2012**, *2*, 1765–1772.
[41] J. Juodkazytė, B. Šebeka, I. Valsiunas, K. Juodkazis, *Electroanalysis* **2005**, *17*, 947–952.
[42] Y. Lee, J. Suntivich, K. J. May, E. E. Perry, Y. Shao-Horn, *J. Phys. Chem. Lett.* **2012**, *3*, 399–404.
[43] N. Mamaca, E. Mayousse, S. Arrii-Clacens, T. W. Napporn, K. Servat, N. Guillet, K. B. Kokoh, *Appl. Catal. B* **2012**, *111*, 376–380.
[44] C. Zhao, E. Yifeng, L. Fan, *Microchim. Acta* **2012**, *178*, 107–114.
[45] L. C. Seitz, C. F. Dickens, K. Nishio, Y. Hikita, J. Montoya, A. Doyle, C. Kirk, A. Vojvodic, H. Y. Hwang, J. K. Norskov, T. F. Jaramillo, *Science (Washington, DC, U.S.)* **2016**, *353*, 1011–1014.
[46] E. Slavcheva, I. Radev, S. Bliznakov, G. Topalov, P. Andreev, E. Budevski, *Electrochim. Acta* **2007**, *52*, 3889–3894.
[47] L. Gong, D. Ren, Y. Deng, B. S. Yeo, *ACS Appl. Mater. Interface* **2016**, *8*, 15985–15990.
[48] J.-B. Jorcin, M. E. Orazem, N. Pébère, B. Tribollet, *Electrochim. Acta* **2006**, *51*, 1473–1479.
[49] T. Grünzel, Y. L. Lee, K. Kuepper, J. Bachmann, J. Beilstein, *Nanotechnology* **2013**, *4*, 655–664.
[50] K. Nielsch, J. Choi, K. Schwirn, R. B. Wehrspohn, U. Gösele, *Nano Lett.* **2002**, *2*, 677–680.

Manuscript received: January 30, 2018
Version of record online: February 27, 2018